

Mechanistically-guided materials chemistry: synthesis of new ternary nitrides, CaZrN_2 and CaHfN_2

Christopher L. Rom,^{†,‡} Andrew Novick,[¶] Matthew J. McDermott,^{§,||} Andrey A. Yakovenko,[⊥] Jessica R. Gallawa,[†] Gia Thinh Tran,[†] Dominic C. Asebiah,[†] Emily N. Storck,[†] Brennan C. McBride,[†] Rebecca C. Miller,[#] Amy L. Prieto,[†] Kristin A. Persson,^{@,||} Eric Toberer,[¶] Vladan Stevanović,[¶] Andriy Zakutayev,[‡] and James R. Neilson^{*,†,Δ}

[†]*Department of Chemistry, Colorado State University, Fort Collins, CO, USA*

[‡]*Materials Science Center, National Renewable Energy Laboratory, Golden, CO, USA*

[¶]*Department of Physics, Colorado School of Mines, Golden, CO, USA*

[§]*Materials Sciences Division, Lawrence Berkeley National Laboratory, Berkeley, CA, USA*

^{||}*Department of Materials Science and Engineering, University of California, Berkeley, CA, USA*

[⊥]*X-ray Science Division, Advanced Photon Source, Argonne National Laboratory, Lemont, IL, USA*

[#]*Analytical Resources Core, Colorado State University, Fort Collins, CO, USA*

[@]*Molecular Foundry, Lawrence Berkeley National Laboratory, Berkeley, CA, USA*

^Δ*School of Advanced Materials Discovery, Colorado State University, Fort Collins, CO, USA*

E-mail: james.neilson@colostate.edu

Abstract

Recent computational studies have predicted many new ternary nitrides, revealing synthetic opportunities in this underexplored phase space. However, synthesizing new ternary nitrides is difficult, in part because intermediate and product phases often have high cohesive energies that inhibit diffusion. Here, we report the synthesis of two new phases, calcium zirconium nitride (CaZrN_2) and calcium hafnium nitride (CaHfN_2), by solid state metathesis reactions between Ca_3N_2 and MCl_4 ($M = \text{Zr, Hf}$). Although the reaction nominally proceeds to the target phases in a 1:1 ratio of the precursors via $\text{Ca}_3\text{N}_2 + \text{MCl}_4 \longrightarrow \text{CaMN}_2 + 2\text{CaCl}_2$, reactions prepared this way result in Ca-poor materials ($\text{Ca}_x\text{M}_{2-x}\text{N}_2$, $x < 1$). A small excess of Ca_3N_2 (ca. 20 mol%) is needed to yield stoichiometric CaMN_2 , as confirmed by high-resolution synchrotron powder X-ray diffraction. *In situ* synchrotron X-ray diffraction studies reveal that nominally stoichiometric reactions produce Zr^{3+} intermediates early in the reaction pathway, and the excess Ca_3N_2 is needed to reoxidize Zr^{3+} intermediates back to the Zr^{4+} oxidation state of CaZrN_2 . Analysis of computationally-derived chemical potential diagrams rationalizes this synthetic approach and its contrast from the synthesis of MgZrN_2 . These findings additionally highlight the utility of *in situ* diffraction studies and computational thermochemistry to provide mechanistic guidance for synthesis.

Introduction

Predictive synthesis remains an important goal for materials chemists.¹⁻³ While many joint computational-experimental synthesis efforts have been reported in literature,⁴⁻¹⁶ trial-and-error approaches remain the dominant paradigm. Within this current paradigm, *in situ* X-ray diffraction (XRD) is a powerful technique for materials discovery.^{15,17-20} Sometimes called “panoramic synthesis,”¹⁷⁻¹⁹ *in situ* X-ray diffraction allows for observation of solid-state reactivity as it happens. Short-lived intermediate species and subtle crystallographic changes can be detected which would otherwise be missed by *ex situ* experiments, accelerating materials discovery. In a move towards predictive synthesis, *in situ* XRD has been used in concert with computationally-generated chemical potential

diagrams²¹ to rationalize polymorph selectivity in the synthesis of ternary oxides²² However, this specific combined approach of *in situ* XRD and chemical potential diagrams has yet to be used to discover new materials.

Nitrides are a compelling class of materials for melding computational guidance with *in situ* X-ray diffraction (XRD) studies because they are difficult to synthesize. High-temperatures are often needed to overcome the relative inertness of N₂ (941 kJ/mol dissociation energy)²³ and drive solid state diffusion.^{24,25} However, elevated temperatures increase the entropic favorability of N₂ gas, which leads many nitrides to decompose at relatively low temperatures.^{26,27} Therefore, successful syntheses may be limited to narrow temperature windows, which *in situ* XRD can help identify.²⁸ Recent computational studies have predicted numerous stable phases in previously uncharted spaces,^{4,11,29–31} accelerating the discovery of new phases (e.g., MgSnN₂,^{32,33} CaSnN₂,³⁴ and MgZrN₂^{35,36}). Yet many predicted phases remain undiscovered, providing copious targets for synthesis.

All of the ABN₂ phases (A = Mg, Ca, Sr, Ba; B = Ti, Zr, Hf) have been synthesized previously,^{35,37–40} with the exception of CaZrN₂ and CaHfN₂.²⁶ As summarized in Figure 1, these phases crystallize with several structure types: rocksalt ($Fm\bar{3}m$), KCoO₂-type ($P4/nmm$), and α -NaFeO₂ ($R\bar{3}m$). Given the intermediate size of Ca²⁺ relative to the other alkali earths (Figure 1),⁴¹ CaZrN₂ and CaHfN₂ were predicted to crystallize in the α -NaFeO₂ structure type.⁴² However, syntheses of CaZrN₂ and CaHfN₂ have not been previously reported, although one group described some synthetic attempts towards these ternaries that yielded only ZrN and HfN.⁴³

Here, we report the discovery of CaZrN₂ and CaHfN₂ in the disordered rocksalt (RS) structure via a metathesis approach. Heating Ca₃N₂ and ZrCl₄ or HfCl₄ up to a high-temperature dwell (ca. 1000 °C) for a brief period of time (10 min) yields CaZrN₂ and CaHfN₂ as fine powders (along with a byproduct CaCl₂). Importantly, a slight excess of Ca₃N₂ is needed, a fact we rationalize based on our *in situ* synchrotron X-ray diffraction studies and computational thermodynamic analysis of the reaction pathway that show reduced Zr³⁺ intermediates. Chemical potential diagrams rationalize the thermodynamics behind the observed reactions, accurately predicting differences

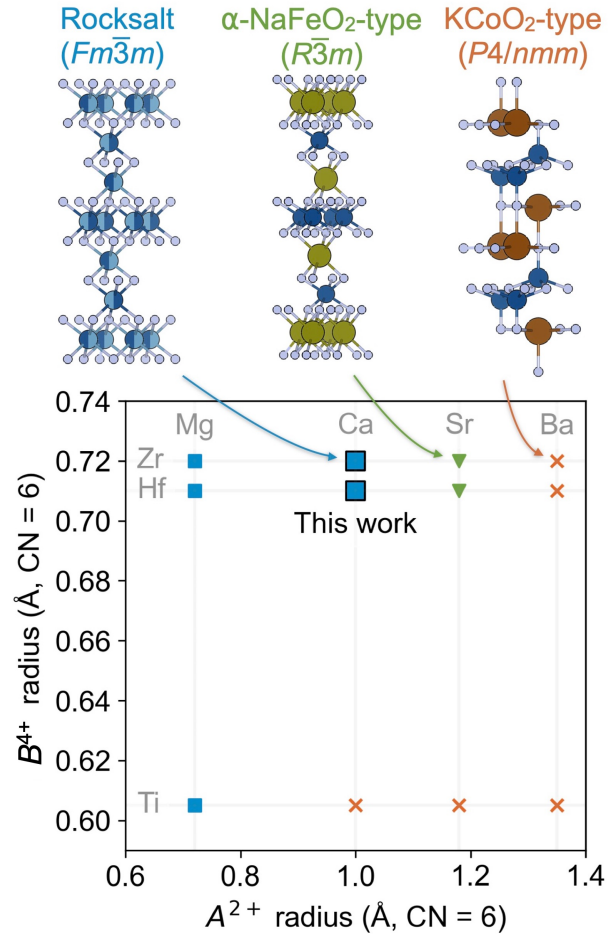


Figure 1: The ABN_2 ternaries with larger alkali earth cations (Sr and Ba) crystallize in cation-ordered phases of the $KCoO_2$ -type and α - $NaFeO_2$ -type structures, while $MgBN_2$ phases take the rocksalt (RS) structure. This work shows that $CaZrN_2$ and $CaHfN_2$ crystallize in the cation-disordered RS structure. Radii are sourced from literature.⁴¹

in the reaction pathway between the reactions targeting $CaZrN_2$ vs. $MgZrN_2$ vs. $ZnZrN_2$ (which has not yet been synthesized in bulk). Additional thermodynamic calculations show that these disordered RS ternaries are metastable (relative to the cation-ordered polymorph) even at the high synthesis temperatures. In sum, these findings show how chemical potential diagrams can augment *in situ* XRD experiments and improve our ability to predict synthesis pathways.

Results and Discussion

Structural and compositional analysis

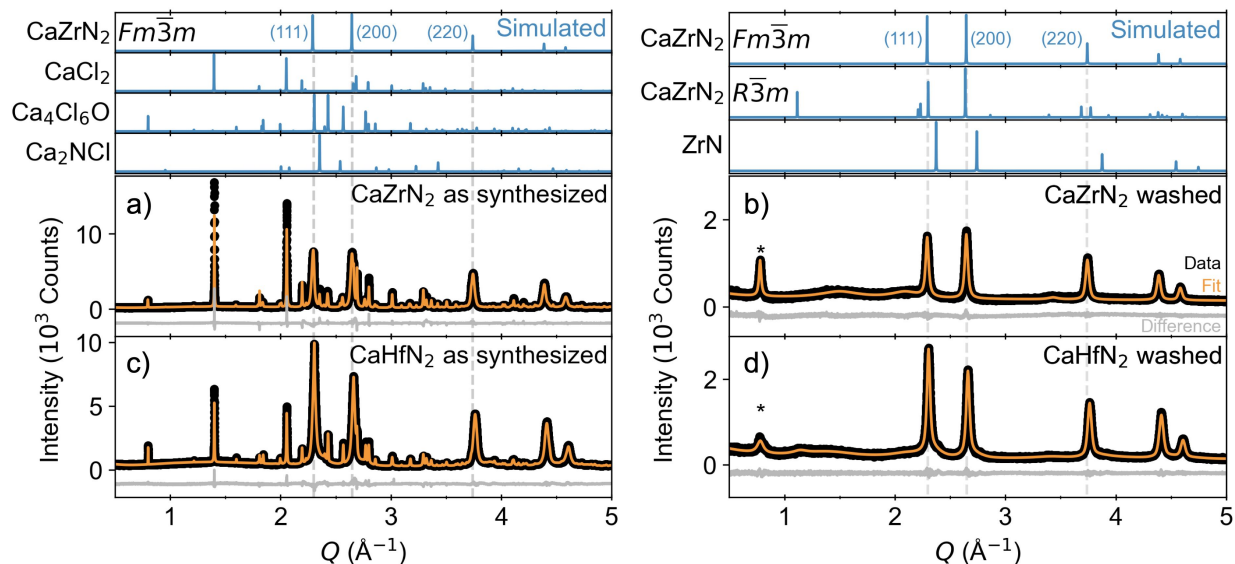


Figure 2: SXRD data of a) CaZrN_2 as synthesized and b) washed along with c) CaHfN_2 as synthesized and d) washed. Simulated patterns for relevant phases are shown for reference (top). The predicted, ordered structure ($R\bar{3}m$) of CaMN_2 was not observed. A single impurity peak appears after washing (marked by *), possibly a disordered $\text{Ca}_4\text{Cl}_6\text{O}$ or calcium methoxide. Dashed gray vertical lines guide the eye to the (111), (200), and (220) reflections of CaMN_2 $Fm\bar{3}m$. Full diffraction patterns are shown in Figure S2, and refinement results are in Tables S1-S2 and Figure S3.

High-resolution synchrotron powder X-ray diffraction (SXRD) measurements show that metathesis reactions between Ca_3N_2 and $M\text{Cl}_4$ ($M = \text{Zr}, \text{Hf}$) yielded CaZrN_2 and CaHfN_2 in the RS structure ($Fm\bar{3}m$, Figure 2). These samples ($1.21 \text{ Ca}_3\text{N}_2 + \text{ZrCl}_4$ and $1.16 \text{ Ca}_3\text{N}_2 + \text{HfCl}_4$) were heated at $+5 \text{ }^\circ\text{C}/\text{min}$ to $1100 \text{ }^\circ\text{C}$, dwelled for 10 min, and then air-quenched to yield CaMN_2 along with an array of side products (CaCl_2 , Ca_2NCl , $\text{Ca}_4\text{Cl}_6\text{O}$, and in the case of $M = \text{Hf}$, trace HfN). Recovered samples were black, red, or green depending on precise synthesis conditions (Figure S1). Washing the samples with anhydrous methanol removes the chloride-containing byproducts (CaCl_2 , Ca_2NCl , $\text{Ca}_4\text{Cl}_6\text{O}$). However, one unindexed diffraction peak is present at $Q = 0.8 \text{ \AA}^{-1}$. This peak matches both the (100) reflection from $\text{Ca}_4\text{Cl}_6\text{O}$ and the most intense reflection in a prior report of calcium methoxide.⁴⁴ Unfortunately, the presence of the impurity phase inhibits

accurate compositional analysis by Scanning Electron Microscopy (SEM) with Energy Dispersive X-ray Spectroscopy (EDS), rigorously air-free X-ray Photoelectron Spectroscopy (XPS), and combustion analysis (further described in the Supporting Information, Figures S5-S8 and Tables S3-S4).⁴⁵⁻⁴⁸ Consequently, our characterization efforts centered on diffraction.

Rietveld analysis of the RS products show these phases are consistent with cation-disordered CaZrN_2 and CaHfN_2 . The metal site occupancy (x in $\text{Ca}_x\text{M}_{2-x}\text{N}_2$) refined to 1.00(2) for the washed CaZrN_2 and 1.00(1) for the washed CaHfN_2 sample. Washing does not substantially change the refined metal site occupancy or lattice parameter compared to the samples as synthesized (Figure S3). Lattice parameters of the washed CaMN_2 phases refined to substantially larger unit values ($a = 4.7486(3)$ Å and $4.7224(4)$ Å for CaZrN_2 and CaHfN_2 , respectively) than their isostructural binaries ($a = 4.58$ Å and 4.52 Å for ZrN and HfN , respectively).^{49,50} These unit cell values are close to the Ca-N-Zr distance in the computationally-predicted, cation-ordered CaZrN_2 structure (4.744 Å), which serves as an estimate for the theoretical disordered RS lattice parameter (Figure S4). We focused most of our work on the Zr analog, since Zr and Hf exhibit analogous chemistry in this case.

A slight excess of Ca_3N_2 (ca. 20 mol%) is required to yield stoichiometric CaZrN_2 (Figure 3), as measured by the product lattice parameter. Although the nominal balanced equation for the reaction is $\text{Ca}_3\text{N}_2 + \text{ZrCl}_4 \longrightarrow \text{CaZrN}_2 + 2 \text{CaCl}_2$, a 1:1 precursor ratio yields a lattice parameter of 4.72 Å, trending towards ZrN and suggesting a Ca-poor phase. With an additional 20 mol% Ca_3N_2 (i.e., $n = 1.20$), the RS lattice parameter is closer to the 4.744 Å value estimated from the computationally-predicted structure (Figure S4). The continued growth in the RS lattice parameter above $n = 1.20$ could suggest the formation of Ca-interstitials, but characterizing such defects is beyond the scope of this study. This trend contrasts with our prior synthesis of MgZrN_2 , where the stoichiometric reaction $2.0 \text{Mg}_2\text{NCl} + \text{ZrCl}_4 \longrightarrow \text{MgZrN}_2 + 3 \text{MgCl}_2$ produced the targeted ternary (RS MgZrN_2), and additional Mg_2NCl did not change the RS lattice parameter or increase Mg content (as measured by SXRD, Inductively Coupled Plasma Atomic Emission Spectroscopy, and Energy Dispersive X-ray Spectroscopy).³⁶ Some of the excess Ca_3N_2 reacts with

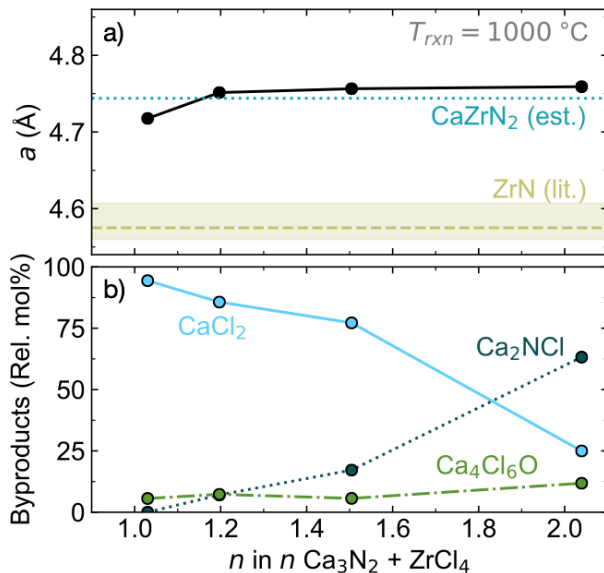


Figure 3: a) The precursor ratio (expressed as n in $n\text{Ca}_3\text{N}_2 + \text{ZrCl}_4$) impacted the lattice parameter of the RS phase and b) the distribution of byproduct phases, as determined by Rietveld analysis. Approximately 20% mole excess ($n = 1.2$) Ca_3N_2 was necessary to yield stoichiometric CaZrN_2 , as indicated by the estimated value of $a = 4.744 \text{ \AA}$ from the computationally-predicted structure (Figure S4). However, some of the excess Ca_3N_2 also yielded a Ca_2NCl byproduct by reacting with CaCl_2 (bottom). The byproduct relative mol% of CaCl_2 , Ca_2NCl , and $\text{Ca}_4\text{Cl}_6\text{O}$ sum to 100% (i.e., $\text{Ca}_x\text{Zr}_{2-x}\text{N}_2$ is not included owing to uncertainty in x). These data were from samples held in alumina crucibles sealed in ampules under vacuum and heated at $5 \text{ }^\circ\text{C}/\text{min}$ to $1000 \text{ }^\circ\text{C}$, dwelled for 10 min, then quenched by removing the ampule from the furnace and placing on the benchtop.

the CaCl_2 byproduct to make Ca_2NCl , which is observed in an increasing mol% with increasing Ca_3N_2 content. The need of excess Ca_3N_2 is not attributable to the oxide impurity in the Ca_3N_2 precursor, which is estimated at $< 5 \text{ wt}\%$ of our precursor by quantitative Rietveld analysis (below the detection limit of laboratory PXRD). We also note that increasing dwell time from 10 min to 4 h did not substantially change the RS lattice parameter, size, or strain for Ca-rich reactions ($2.0 \text{ Ca}_3\text{N}_2 + \text{ZrCl}_4$, $T_{\text{rxn}} = 1000 \text{ }^\circ\text{C}$, Figure S10). Increasing temperature decreases the lattice parameter but increases the crystallite size ($1.2 \text{ Ca}_3\text{N}_2 + \text{ZrCl}_4$, dwell time = 10 min, Figure S11). Furthermore, increasing dwell times for Ca-poor reactions decreases the rocksalt lattice parameter (dwell temperature = $900 \text{ }^\circ\text{C}$, Figure S12). The key observation is that some excess Ca_3N_2 is necessary. This result is explained by observations from our *in situ* SXRD measurements, as discussed in the next section.

Using metathesis (ion exchange) reactions is also a key synthetic choice for the synthesis of CaZrN_2 , as this process circumvents the solid-state diffusion challenges common to traditional ceramic syntheses.^{51,52} A control reaction between Ca_3N_2 and Zr under flowing N_2 at 1000 °C for 10 h produces only ZrN alongside unreacted Ca_3N_2 , indicating that Ca diffusion into the ZrN is slow (Figure S13). Literature also shows the difficulty of making CaZrN_2 and CaHfN_2 . In their report on the synthesis of Ca_4TiN_4 and Ca_5NbN_5 with the assistance of a Li_3N flux, Hunting, et al., noted that similar reactions between Ca_3N_2 and Zr or Hf powders in Li_3N flux only yielded the ZrN and HfN.⁴³ And although many closely related compounds have been synthesized by ceramic techniques (i.e., CaTiN_2 , SrZrN_2 , BaZrN_2),^{37,39,53} the absence of CaZrN_2 and CaHfN_2 from the literature implies that a synthetic strategy had previously been elusive.

We acknowledge that the *perfectly stoichiometric* compounds CaZrN_2 and CaHfN_2 may not be synthesized from the reactions, $1.21 \text{ Ca}_3\text{N}_2 + \text{ZrCl}_4$ and $1.16 \text{ Ca}_3\text{N}_2 + \text{HfCl}_4$; however, these were the optimal reaction conditions identified in this study. These synthesis conditions produced RS structures most consistent with the title compounds, given our structural analysis of lattice parameter and cation site occupancy. Detailed compositional analysis was not possible with our current samples given an unidentified impurity phase (See the Supporting Information, Figures S5-S8 and Tables S3-S4). Precise analysis of composition (including defects) will be essential for better understanding the potential applications of these new semiconductors, but such analysis is beyond the scope of this study. Instead, we focus on the mechanisms of this synthesis, with the goal of showing how *in situ* SXRD studies and thermodynamic calculations can guide metathesis reactions for the synthesis of elusive new materials.

***In situ* synchrotron powder X-ray diffraction**

In situ synchrotron powder X-ray diffraction studies (SXRD) at the Advanced Photon Source (17-BM) reveals the pathway through which the metathesis reactions proceed. We examined reactions in sealed quartz capillaries targeting CaZrN_2 (and MgZrN_2 , for comparison) starting from reagent mixtures for the ideal reactions: $A_3\text{N}_2 + \text{ZrCl}_4 \longrightarrow A\text{ZrN}_2 + 2 \text{ ACl}_2$ and $2 A_2\text{NCl} + \text{ZrCl}_4 \longrightarrow$

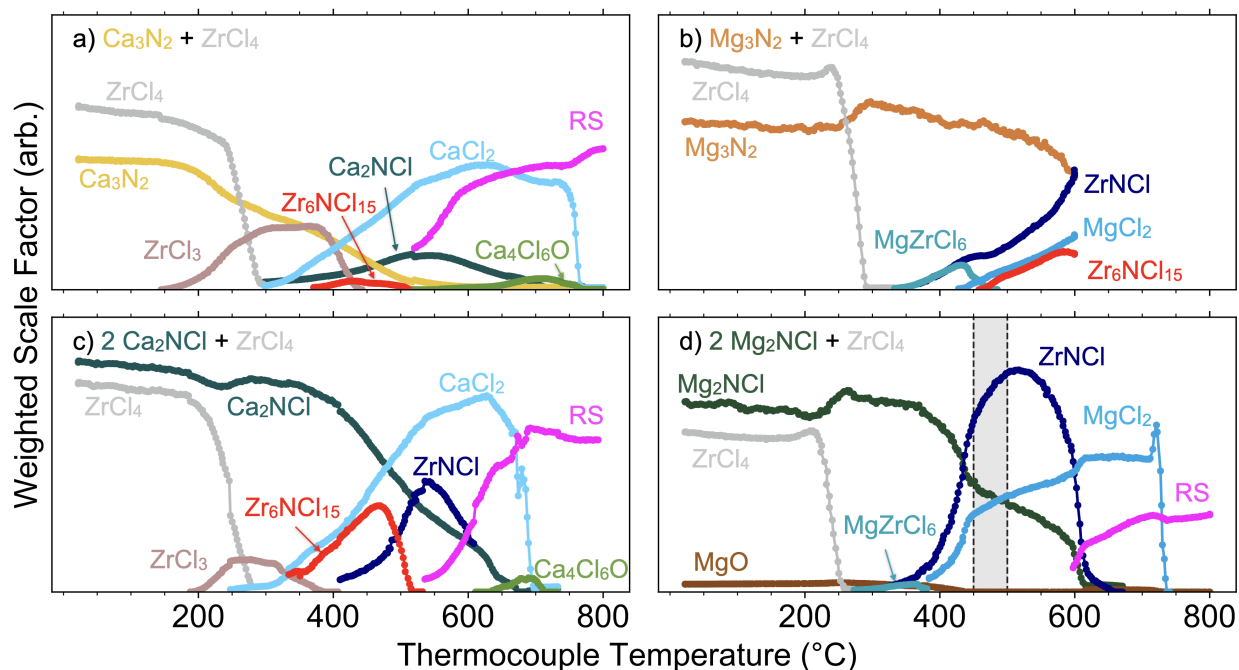
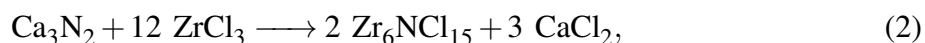
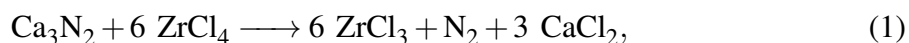


Figure 4: Phase contributions to the *in situ* SXRD data as a function of temperature as indicated by the weighted scale factors (W.S.F.) for reactants, intermediates, and products upon heating precursor mixtures of a) $\text{Ca}_3\text{N}_2 + \text{ZrCl}_4$, b) $\text{Mg}_3\text{N}_2 + \text{ZrCl}_4$, c) $2 \text{Ca}_2\text{NCl} + \text{ZrCl}_4$, and d) $2 \text{Mg}_2\text{NCl} + \text{ZrCl}_4$. In reactions with Mg_3N_2 , Ca_3N_2 , and Ca_2NCl , trivalent Zr species were observed (ZrCl_3 and $\text{Zr}_6\text{NCl}_{15}$), indicating reduction of Zr^{4+} to Zr^{3+} and loss of N_2 . Only the reaction using Mg_2NCl maintained the tetravalent oxidation state of Zr. The ternary phases $\text{Ca}_x\text{Zr}_{2-x}\text{N}_2$ and $\text{Mg}_x\text{Zr}_{2-x}\text{N}_2$ are denoted as “RS”. The grey highlighted region of (d) shows the temperature range used for step 1 of the two-step synthesis of MgZrN_2 detailed in prior reports.^{36,54}

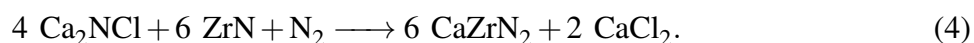
$\text{AZrN}_2 + 3 \text{ACl}_2$ ($A = \text{Mg}, \text{Ca}$). These ratios are calcium-deficient compared to the optimized synthesis of CaZrN_2 discussed previously, yet are nonetheless illuminating. They show how ostensibly similar precursors (A_3N_2 and A_2NCl) proceed via different reaction pathways. These differences in reaction pathway ultimately required different synthetic conditions for the optimized syntheses of MgZrN_2 and CaZrN_2 . The relative amounts of crystalline phases present during the reaction (determined by quantitative phase analysis using the Rietveld method of *in situ* diffraction data) are shown in Figure 4, with the raw diffraction patterns shown in Figures S17 and S18. The observed Zr-containing intermediates are summarized in Table 1.

Quantitative phase analysis of *in situ* SXRD data from the reaction between $\text{Ca}_3\text{N}_2 + \text{ZrCl}_4$ show that reduced Zr^{3+} species form at low reaction temperatures (Figure 4a). ZrCl_3 is the first

intermediate to form, appearing by 200 °C. Subsequently, ZrCl_4 disappears from the patterns as it sublimes ($T_{\text{sub}} = 331$ °C), at which point CaCl_2 begins to grow in. Near 400 °C, the ZrCl_3 converts to a nitride chloride, $\text{Zr}_6\text{NCl}_{15}$. Throughout this process, the Ca_3N_2 precursor steadily declines. Ca_3N_2 is fully consumed by 600 °C, with some of it reacting with the CaCl_2 byproduct to make Ca_2NCl ($\text{Ca}_3\text{N}_2 + \text{CaCl}_2 \longrightarrow 2 \text{Ca}_2\text{NCl}$). Ca_2NCl persists up to 700 °C. By ca. 550 °C, the RS phase $\text{Ca}_x\text{Zr}_{2-x}\text{N}_2$ begins to grow in (initially as ZrN , as will be detailed subsequently). A minor phase of $\text{Ca}_4\text{Cl}_6\text{O}$ also grows in, indicating a small degree of oxygen impurity. The reaction of $2 \text{Ca}_2\text{NCl} + \text{ZrCl}_4$ proceeds in a similar fashion as $\text{Ca}_3\text{N}_2 + \text{ZrCl}_4$. However, using Ca_2NCl also includes a ZrNCl -like intermediate, which is not detected in the Ca_3N_2 reaction (Figure S17). In sum, the initial reaction between $\text{Ca}_3\text{N}_2 + \text{ZrCl}_4$ proceeds through Zr^{3+} intermediates via the following balanced equations:

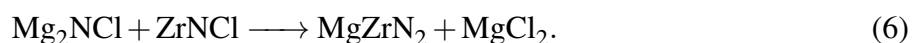


The final step of this process involves the reaction of the Ca_2NCl intermediate with the ZrN rocksalt phase:



In contrast, the analysis of *in situ* SXRD data in the analogous Mg system shows reactivity differences between Mg_3N_2 and Mg_2NCl , with Mg_2NCl conserving the tetravalent state of Zr^{4+} throughout the reaction pathway (Figure 4b and d, Table 1). The observed reaction pathways are consistent with our prior (lower resolution) *in situ* study on the synthesis of MgZrN_2 .³⁶ Both the reaction of $\text{Mg}_3\text{N}_2 + \text{ZrCl}_4$ and the reaction of $2\text{Mg}_2\text{NCl} + \text{ZrCl}_4$ begin with ZrCl_4 sublimation, followed by the formation of a small amount of MgZrCl_6 near 300 °C. However, the reaction with Mg_3N_2 goes on to produce $\text{Zr}_6\text{NCl}_{15}$ near 430 °C, which indicates the reduction of Zr^{4+} to Zr^{3+} , likely paired with the production of N_2 . Furthermore, the amount of Mg_3N_2 only decreases slightly

by 600 °C (at which point, the measurement was stopped). This result suggests that Mg₃N₂ is a kinetically slow precursor. On the other hand, the Mg₂NCl reaction does not produce any distinct Zr³⁺ intermediates. Instead, the amount of Mg₂NCl decreases in a stepwise fashion near 440 °C coincident with the formation of ZrNCl and the rapid increase of MgCl₂. A second stepwise decrease in Mg₂NCl occurs near 600 °C, coincident with the consumption of the ZrNCl and the formation of the RS phase (Mg_xZr_{2-x}N₂). Therefore, the synthesis of MgZrN₂ appears to proceed through two reaction steps:



As noted in prior reports, heating directly to a high temperature (ca. 800 °C) results in an Mg-poor RS phase, but a two-step process yields stoichiometric MgZrN₂.^{36,54} The first step of that two-step process (T_{react}) is a 12 to 24 h dwell at 450–500 °C (the highlighted grey temperature region in Figure 4), likely where Equations 5 and 6 proceed to completion. The second heating step (to $T_{\text{cryst}} = 800$ °C) aids in the crystallization of the amorphous/nanocrystalline MgZrN₂. This *in situ* study reveals how the two-step process allows the synthesis of MgZrN₂ to proceed through a single Zr⁴⁺ intermediate, whereas the synthesis of CaZrN₂ must proceed through Zr³⁺ intermediates that require subsequent re-oxidation (Table 1).

Table 1: Summary of Zr-containing intermediates via the *in situ* SXRD studies shown in Figure 4

Reaction	Zr-containing intermediates			
Ca ₃ N ₂ + ZrCl ₄	ZrCl ₃	Zr ₆ NCl ₁₅		
2 Ca ₂ NCl + ZrCl ₄	ZrCl ₃	Zr ₆ NCl ₁₅	ZrNCl	
Mg ₃ N ₂ + ZrCl ₄		Zr ₆ NCl ₁₅	ZrNCl	MgZrCl ₆
2 Mg ₂ NCl + ZrCl ₄			ZrNCl	MgZrCl ₆

The lattice parameter, a , of the disordered rocksalt Ca_xZr_{2-x}N₂ formed during the Ca₃N₂ + ZrCl₄ reaction shows that the ZrN intermediate from Equation 3 reacts with Ca₂NCl to form CaZrN₂ (Figure 5). As the RS phase grows in between 500 and 600 °C, the lattice parameter

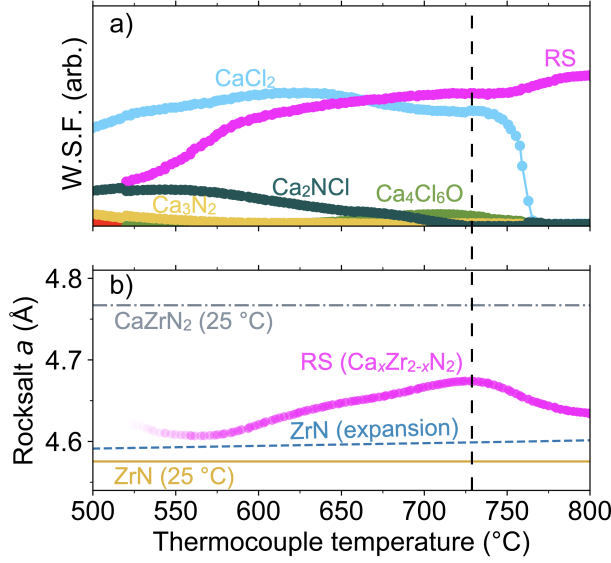
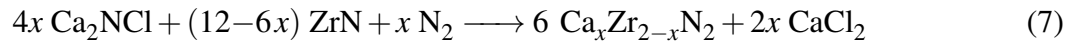


Figure 5: a) Weighted scale factor (W.S.F.) as a function of temperature for the $\text{Ca}_3\text{N}_2 + \text{ZrCl}_4$ reaction and b) refined lattice parameter a for the RS $\text{Ca}_x\text{Zr}_{2-x}\text{N}_2$ obtained from Rietveld analysis of the *in situ* SXR data. The opacity of the RS markers in (b) is normalized to the W.S.F. in (a). The lattice parameters for ZrN and CaZrN_2 at room temperature are shown for reference, along with the value of ZrN accounting for thermal expansion.⁵⁵ The increase in a for $\text{Ca}_x\text{Zr}_{2-x}\text{N}_2$ suggests Ca uptake from the Ca_2NCl intermediate. When the Ca_2NCl intermediate is fully consumed (vertical dashed line), the RS lattice parameter begins contracting, suggesting Ca loss.

closely matches the value expected for ZrN by thermal expansion.⁵⁵ Between 520 °C and 570 °C, the apparent decrease in the parameter is an artifact of the broad, low-intensity peaks that are difficult to accurately fit. Above 570 °C, the parameter expands up to 4.674 Å by 725 °C. The expansion concomitant with the decreasing W.S.F. of Ca_2NCl suggests calcium uptake by ZrN from the Ca_2NCl intermediate across a solid solution $\text{Ca}_x\text{Zr}_{2-x}\text{N}_2$ ($0 \leq x \leq 1$), with Zr^{3+} to Zr^{4+} oxidation driven by N_2 reincorporation:



Above 725 °C, the RS lattice parameter decreases. This inflection point occurs at the same temperature at which Ca_2NCl is fully consumed. The contraction of the lattice parameter is consistent with a loss of calcium from the structure, possibly by reaction with oxygen from the quartz container ($2 \text{Ca}_x\text{Zr}_{2-x}\text{N}_2 + x \text{SiO}_2 \longrightarrow 2x \text{CaO} + (4-2x) \text{ZrN} + x \text{N}_2 + x \text{Si}$).

This pathway shows why “excess” Ca_3N_2 is required for CaZrN_2 formation: it provides the necessary oxidant, N_2 . The N_2 likely comes from the reincorporation of the released nitrogen yielded during Zr^{3+} formation (Equation 1), although alternative hypotheses are considered in the Supporting Information (Equations S1 and S2). While this process may seem similar to the ceramic reaction discussed previously (Figure S13), the ZrN crystallites formed *in situ* via metathesis are very small (ca. 10 nm) compared to the ZrN formed via the ceramic route (ca. 1 μm) and may contain a significant fraction of point defects, facilitating diffusion. These differences allow the metathesis-produced ZrN to react to form CaZrN_2 within a 10 min dwell while the ceramic route is impractically slow. To test the Equation 7 hypothesis, we reacted $2 \text{Ca}_3\text{N}_2 + \text{ZrCl}_4$ at 1000 °C under flowing N_2 for 4 h (Figure S13). The resulting PXRD data of the red powder was well described by rocksalt CaZrN_2 ($a = 4.764 \text{ \AA}$) with Ca_2NCl as the only byproduct. Furthermore, thermodynamic calculations (see next section) suggest Equation 7 is a thermodynamically favorable step.

Thermodynamic analysis of the reaction pathway

The chemical potential diagrams shown in Figure 6 describe the energetic landscape through which these metathesis reactions proceed. These models are computed using calculated phase energies from the Materials Project database⁵⁶ (see Methods). Each visible facet is a stable phase in the A-Zr-Cl system; larger facets indicate phases with deeper stability on the convex hull of a compositional phase diagram relative to competing phases. Nitrogen-containing phases are illustrated by 3-dimensional (A-Zr-Cl) polyhedral slices of the full 4-dimensional polytopes. Intersection points, edges, or faces between these regions of chemical potential space indicate which phases share stable interfaces. It has previously been observed that a chemical reaction proceeding under local equilibrium (i.e., diffusion-controlled) conditions will follow a pathway between adjacent phases.^{2,22}

Figure 6a and c show that no Zr^{4+} -containing species in the Ca-Zr-N-Cl phase space shares a stable interface with the CaZrN_2 product, indicating that Zr^{3+} -containing intermediates must

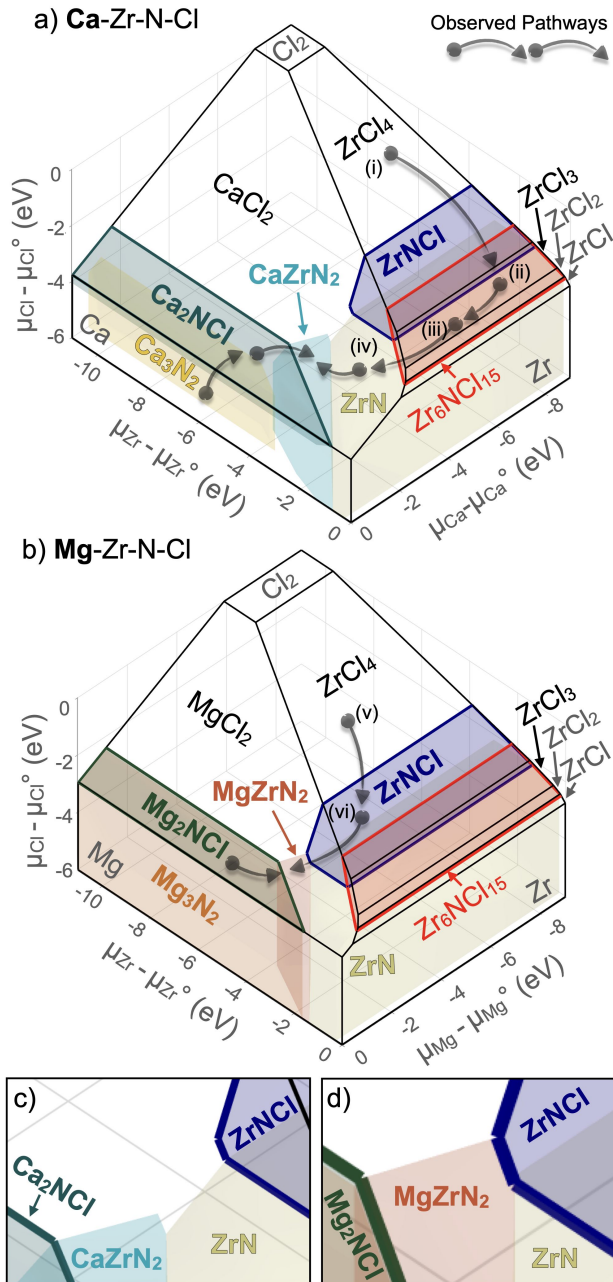


Figure 6: Chemical potential diagrams for a) the Ca-Zr-N-Cl chemical system and b) the Mg-Zr-N-Cl chemical system calculated for 300 °C. Focused view highlighting the interfaces between ZrNCl and c) Ca_2NCl or d) Mg_2NCl . Select nitrogen-containing phases in the 4-component system are illustrated via their intersection with the 3-dimensional $\mu_{\text{Ca}} - \mu_{\text{Zr}} - \mu_{\text{Cl}}$ or $\mu_{\text{Mg}} - \mu_{\text{Zr}} - \mu_{\text{Cl}}$ spaces. These intersections may appear with complicated volumes due to the lower dimensional intersection (e.g., CaZrN_2 , ZrN). Full quaternary diagrams are shown in Figure S22. Curved arrows qualitatively illustrate the experimentally observed reaction pathways.

form if the system proceeds through local equilibrium at interfaces. Specifically, the region of stability for ZrN connects both the $\text{Zr}_6\text{NCl}_{15}$ and ZrNCl spaces to the CaZrN_2 space, indicating that ZrN should form along the pathway to CaZrN_2 . In reality, due to the accommodation of off-stoichiometry, there is likely no sharp boundary (discontinuity) between ZrN and CaZrN_2 .²¹ Rather, this sharp transition is due to the limitations of our thermodynamic data, as only ordered, stoichiometric compounds are permitted in the DFT calculations of the Materials Project database. We discuss the stability of cation-disordered CaZrN_2 further in the next section and in the Supporting Information (Figure S21).

The chemical potential diagram for the Mg-Zr-N-Cl system (Figure 6b) appears similar to the Ca system but with one key difference: ZrNCl shares a stable interface with both the precursor ZrCl_4 and the product MgZrN_2 (Figure 6d). This shared boundary suggests that the intermediate ZrNCl (a Zr^{4+} -containing phase) facilitates the formation of MgZrN_2 at the $\text{ZrCl}_4|\text{Mg}_2\text{NCl}$ interface while preventing the system from undergoing Zr and N-based reduction and oxidation.

Reaction network analysis⁵⁷ can quantify these differences between the Ca- and Mg-Zr-N-Cl systems. The method calculates a distance in chemical potential space, simplifying these geometric representations into numeric values. The chemical potential distance for the reaction of $\text{Ca}_2\text{NCl} + \text{ZrNCl} \longrightarrow \text{CaZrN}_2 + \text{CaCl}_2$ is 0.733 eV/atom, where the non-zero number means that the reactants and products do not share stable interfaces (as visualized in Figure 6c). In contrast, $\text{Mg}_2\text{NCl} + \text{ZrNCl} \longrightarrow \text{MgZrN}_2 + \text{MgCl}_2$ (Figure 6d) has a chemical potential distance of 0.033 eV/atom, which is only non-zero because of how metastable phases like Mg_2NCl are calculated. Further details are in the Supporting Information (Tables S5-S13).

The chemical potential diagram boundaries are consistent with the *in situ* SXRD measurements. For the Ca-system, the annotated reaction arrows in Figure 6a correspond to the intermediates observed to form by *in situ* SXRD (Figure 4), and the progression from ZrN to CaZrN_2 via a $\text{Ca}_x\text{Zr}_{2-x}\text{N}_2$ solid solution (Figure 5): arrow (i) represents Equation 1, arrow (ii) Equation 2, arrow (iii) Equation 3, and arrow (iv) Equation 4 (or an alternative hypothesis, Equations S1, S2). Similarly, the chemical potential diagram for the Mg-system also matches the observed behavior

of the $\text{Mg}_2\text{NCl} + \text{ZrCl}_4$ reaction: arrow (v) represents Equation 5 and arrow (vi) Equation 6.

This mechanistic guidance provided the key insight that ultimately led to our successful syntheses. As the Ca-Zr-N-Cl chemical potential diagram (Figure 6a, c) shows that ZrN formation is unavoidable along the path to CaZrN_2 , we changed our synthesis conditions (relative to the two-step synthesis of MgZrN_2)³⁶ to deal with the refractory ZrN intermediate. Specifically, we used Ca_3N_2 in slight excess to provide an oxidant, and we increased our reaction temperature to increase diffusion. We also used only one heating step, as a low temperature step would not avoid Zr^{4+} reduction (whereas in the case of MgZrN_2 , the two-step process maintained the oxidation state of Zr^{4+}).³⁶ These changes led to the successful syntheses shown in Figure 2.

Importantly, these chemical potential diagrams can also be used to identify thermodynamically disfavored reactions, allowing researchers to quickly move beyond systems that are unlikely to work. To demonstrate this point, we also conducted metathesis syntheses and thermodynamic calculations targeting ZnZrN_2 from 1.2 $\text{Zn}_3\text{N}_2 + \text{ZrCl}_4$ and 2.4 $\text{Zn}_2\text{NCl} + \text{ZrCl}_4$ (Figures S19 and S20). ZnZrN_2 has been synthesized via combinatorial sputtering of thin films¹⁴ but has not yet been synthesized in bulk. Our *in situ* SXRD experiments and thermodynamic analysis reveal that the phase is unlikely to be synthesized via metathesis without significantly increasing μ_{N} . The chemical potential diagrams calculated as a function of temperature show that while ZnZrN_2 is predicted to be stable at room temperature, it becomes destabilized at the more synthetically relevant temperature of 300 °C (Figure S19). Instead, ZrNCl and ZrN are calculated to be the main thermodynamic products. *In situ* SXRD measurements confirm these predictions (Figure S20). Although these calculations do not rule-out the possibility of ZnZrN_2 forming as a kinetic product, they do show that reactions proceeding through local thermodynamic equilibrium at elevated temperature and ambient N_2 pressure will not yield the targeted phase. These chemical potential diagrams therefore serve as powerful tools to accelerate materials discovery via mechanistically guided synthesis.

Several shortcomings limit the predictive ability of chemical potential diagrams. First, chemical potential diagrams with > 3 dimensions may obscure certain phases: the 4-dimensional chem-

ical potential diagrams shown here are only visualized in 3-dimensions of chemical potential (μ_A , μ_{Zr} , and μ_{Cl}) with *select* N-containing phases shown as intersections with the 3-dimensional space. Fortunately, quaternary compositional phase diagrams provide a complementary and complete, but complicated, visualization (Figure S22). The geometric distances for n -dimensional chemical spaces can also be calculated numerically using reaction network analysis⁵⁷ as further discussed in the Supporting Information (Tables S5-S14). Chemical potential diagrams also lack true kinetic information; they can only illustrate effective kinetic barriers provided by the need of a reaction to form an additional intermediate phase to establish local equilibrium.² Lastly, they are limited by the phases in the computational databases (e.g., the Materials Project). These databases, while large and growing larger, are incomplete.⁴ They also only contain ordered phases (not the disordered structures we observe).

Metastability of cation disorder in CaZrN_2

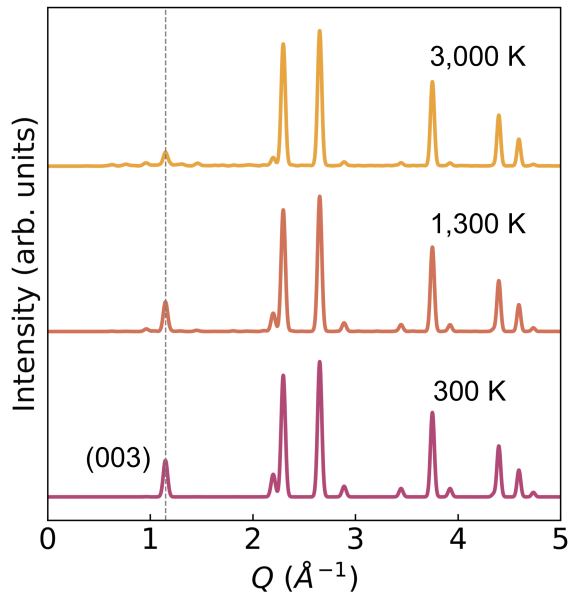


Figure 7: Simulated diffraction patterns for the thermodynamic ground state of CaZrN_2 , calculated as a function of temperature from the ensemble average. The supercell reflection at $Q = 1.1 \text{ \AA}^{-1}$ corresponding to the (003) plane of the fully ordered ($R\bar{3}m$) structure persists even up to 3,000 K.

The observed disorder in CaZrN_2 is counter-intuitive. The large contrast in atomic radii be-

tween Ca^{2+} and Zr^{4+} (1.00 Å and 0.72 Å, respectively)⁴¹ should favor cation ordering as observed in CaTiN_2 , SrZrN_2 , and BaZrN_2 .^{37,39,53} Indeed, through the use of DFT and cluster expansion, we found that the ground state configuration is strongly favored at 1,300 K (Figure S21). If CaZrN_2 were in thermodynamic equilibrium, there would be an insignificant degree of cation disorder.

To relate these predictions to experimental observations, we simulated PXRD patterns across all 24-atom configurations and ensemble averaged them for the temperatures of interest (Figure 7). As expected for increasing disorder, the reflection from the (003) plane in the ordered structure (arising from cation layering) decays in intensity with increasing temperature. Temperatures generated from DFT can be offset a couple hundred degrees from experiment,⁵⁸ but the range from 300 to 3,000 K safely encompasses the synthesis temperature of 1,300K. The (003) peak in the simulated patterns is significant even at 3,000 K, suggesting that the ordering in CaZrN_2 would be observed in the XRD pattern if the system were fully in thermodynamic equilibrium.

The SXRD pattern of the experimentally synthesized CaZrN_2 does not show this low-angle peak (Figure 2), indicating that this cation-disordered CaZrN_2 is far from thermodynamic equilibrium. This hypothesis can be supported due to the short synthesis times relative to the slow rate of diffusion in nitrides.⁵⁹ Here we demonstrate an instance of a short metathesis reaction kinetically trapping disorder in a ternary nitride. Further annealing or higher synthesis temperatures could produce cation ordering in CaZrN_2 , as seen in ZnGeN_2 and ZnGeP_2 .^{60,61}

This finding highlights that accounting for metastability is an area of further growth for predictive synthesis. As with thin film sputtering,¹⁴ bulk syntheses involve myriad thermodynamic and kinetic factors that influence final product formation. While computational techniques to account for temperature effects on enthalpy have been developed,⁶² entropic contributions (e.g., compositional and configurational disorder) are not yet included in these chemical potential diagrams as they are computationally expensive to calculate. This gap motivates further work aligning computational and synthetic techniques to bring about a truly predictive synthesis paradigm.

Conclusion

We report the discovery of two new ternary nitrides, CaZrN_2 and CaHfN_2 , via mechanistically-guided metathesis synthesis of bulk powders. These phases crystallize in the cation-disordered RS structure ($Fm\bar{3}m$), as opposed to the computationally-predicted $\alpha\text{-NaFeO}_2$ structure type ($R\bar{3}m$). *In situ* synchrotron powder X-ray diffraction analysis shows how Zr^{3+} intermediates form early on in the reaction process, which rationalizes why excess of the Ca_3N_2 reagent is synthetically necessary to generate a higher chemical potential of nitrogen. These findings stand in contrast to our prior synthesis of MgZrN_2 , which proceeds stoichiometrically from $2 \text{Mg}_2\text{NCl} + \text{ZrCl}_4$ to $\text{MgZrN}_2 + 2 \text{MgCl}_2$ via a ZrNCl intermediate, as to avoid any $\text{N}_2(\text{g})$ linked redox chemistry. The observed synthetic pathways match well with the predictions generated from chemical potential diagrams. Additional thermodynamic calculations show that the observed $Fm\bar{3}m$ structure is metastable with respect to the ordered $R\bar{3}m$ structure, suggesting that the $R\bar{3}m$ structure may be achievable under different synthetic conditions. In sum, these findings demonstrate a generalizable strategy for predicting and conducting metathesis reactions with the goal of synthesizing new ternary nitrides: combine *in situ* SXRD studies with thermodynamic calculations for mechanistically-guided materials chemistry.

Methods

Synthesis

Caution: N_2 gas formation within sealed ampules can cause explosions at high temperatures, and appropriate precautions should be taken to prevent equipment damage and unsafe conditions.

All reagents are moisture-sensitive, and were therefore handled in an argon-filled glovebox unless otherwise noted ($\text{O}_2 < 0.1 \text{ ppm}$, $\text{H}_2\text{O} < 0.5 \text{ ppm}$). Ca_3N_2 (Chem Cruz or Alfa Aesar, $>98\%$ metals basis), Mg_3N_2 (Alfa Aesar, $>98\%$ metals basis), and MgCl_2 (Sigma Aldrich, anhydrous, $>98\%$ metals basis) were used as received. ZrCl_4 (Acros, 98%) and HfCl_4 (Sigma Aldrich, 99% metals

basis, except for Zr, with $< 2.7\%$) were purified by heating approximately 4 g in a sealed quartz ampule (10 mm inner diameter, 12 mm outer diameter, ca. 30 cm long) in a 3-zone horizontal tube furnace to transport ZrCl_4 from the hot zone (400 °C) to the colder zone (300 °C), leaving behind less volatile, oxide-based impurities (e.g., ZrO_2). CaCl_2 (anhydrous, Alfa Aesar, 98%) was dried under flowing Ar for 24 h at 300 °C.

Ca_2NCl was synthesized following a method adapted from literature.⁶³ Stoichiometric amounts of Ca_3N_2 and CaCl_2 were combined in an agate mortar and pestle and ground into a homogeneous pink powder (ca. 2 g). The powder was then cold pressed ($P \approx 300$ MPa) into a dense pellet (diameter = 0.25 in) and placed in a niobium tube (10 cm long, 0.375 inch outer diameter, 0.015 inch wall thickness). Prior to use, the surface oxide of the niobium was removed by scrubbing with an abrasive scour pad in the glovebox. The ends of the tube were crimped down using the arbor press. This ampule was then brought out of the glovebox and quickly sealed under an argon atmosphere via arc-melting of the crimped ends of the niobium. The sealed metal ampule was then sealed in a quartz ampule under vacuum and heated at 5 °C/min in a muffle furnace to a set point of 740 °C. The reaction was held at temperature for 50 h, and then allowed to cool to room temperature before opening the ampule in the glovebox.

Mg_2NCl was synthesized following a method adapted from literature,⁶⁴ as we described previously.³⁶ Stoichiometric amounts of Mg_3N_2 (ca. 3 g) and MgCl_2 (ca. 3 g) were combined in an agate mortar and pestle and ground into a homogeneous tan powder. The powder was then cold pressed ($P \approx 80$ MPa) into a dense pellet (diameter = 0.5 in) and placed in a quartz ampule (14 mm i.d., 16 mm o.d.). This ampule was then brought out of the glovebox and quickly sealed under vacuum (≤ 20 mTorr, as determined by a Pirani gauge) by using an oxygen/methane torch. The sealed ampule (ca. 15 cm³ internal volume) was then heated at 10 °C/min in a muffle furnace to a set point of 550 °C. The reaction was held at temperature for 5 days and then allowed to cool to room temperature before opening the ampule in the glovebox.

Reaction mixtures targeting CaZrN_2 and CaHfN_2 were prepared by combining the desired reagents in specific mole ratios (e.g., 1.17 $\text{Ca}_3\text{N}_2 + \text{ZrCl}_4$, as specified in the text) and homoge-

nizing with an agate mortar and pestle. Reaction scales ranged from ca. 50 mg to ca. 500 mg total charge of reactants. Reaction mixtures were loaded into crucibles as loose powders or as 0.25 inch diameter pellets (cold pressed at 300 MPa) and sealed under vacuum in quartz ampules (< 30 mTorr). Many syntheses were conducted using alumina crucibles, but optimized syntheses used homemade stainless steel crucibles to minimize oxygen contamination. These steel crucibles were made from stainless steel tubes (3/8 in outer diameter, 0.020 in wall thickness, TP-304L), welded closed on one end and left open on the other. The optimized synthesis involved pelletized reaction mixtures (ca. 500 mg) held in the steel crucibles nested inside quartz ampules along with a 1 g graphite rod as an oxygen getter, physically separated from the pellet. These ampules were transferred from the glovebox to a vacuum manifold using a custom air-free transfer valve, and sealed flame-sealed under vacuum (< 30 mTorr) using an oxygen/methane torch. Optimized reactions were heated in a muffle furnace at $+5$ °C/min to the specified dwell temperature, allowed to thermally equilibrate for 10 min, and then air-quenched by removing the ampule from the furnace and placing it in an insulating brick holder on the benchtop. Other synthesis conditions are specified in the text where relevant. The products are moisture sensitive. To remove byproduct CaCl_2 from the target compounds, samples were washed with anhydrous methanol (dried over molecular sieves for at least five days)⁶⁵ in an argon glovebox.

X-ray diffraction experiments

The products of all reactions were characterized by powder X-ray diffraction (PXRD). PXRD measurements were performed by using a Bruker DaVinci diffractometer with $\text{Cu K}\alpha$ X-ray radiation. Prior to collecting PXRD, silicon powder was ground in with the reaction products as an internal standard for lattice parameters. All samples were prepared for PXRD from within the glovebox by placing powder on off-axis cut silicon single crystal wafers to reduce the background and then covered with polyimide tape to slow exposure to the atmosphere.

High-resolution synchrotron powder X-ray diffraction (SXRD) measurements on select samples were conducted via the mail-in program at the 11-BM-B end station of the Advanced Photon

Source at Argonne National Laboratory.⁶⁶ Samples were prepared loading reaction products (from optimized synthetic conditions) into extruded quartz capillaries (0.69 mm inner diameter, 0.7 mm outer diameter), which were subsequently nested inside kapton capillaries for measurement. Data were collected at $\lambda \approx 0.459 \text{ \AA}$. SXR D patterns are shown in Q -space to account for small difference in wavelength between measurements ($Q = 4\pi \sin(\theta)/\lambda$).

In situ SXR D were conducted at the 17-BM-B end station of the Advanced Photon Source at Argonne National Laboratory ($\lambda = 0.24101 \text{ \AA}$). Samples were prepared by loading reaction mixtures into extruded quartz capillaries (0.9 mm inner diameter, 1.1 mm outer diameter) and flame-sealing under vacuum ($< 30 \text{ mTorr}$). Capillaries were loaded into a flow-cell apparatus⁶⁷ and heated at $5 \text{ }^\circ\text{C}/\text{min}$ to the specified temperature. *Caution: N_2 gas formation within the capillary can cause it to break at high temperatures.* Diffraction pattern images were collected using a PerkinElmer plate detector positioned 700 mm away from the sample. Images were collected every 30 s by summing 20 exposures of 0.5 s each, followed by 20 s of deadtime. Images collected from the plate detector were radially integrated using GSAS-II and calibrated using a silicon standard.

X-ray diffraction analysis

Quantitative phase analysis of PXR D and *in situ* SXR D data was conducted using the Rietveld method as implemented in TOPAS v6.⁴⁷ For laboratory-diffraction PXR D experiments (Bruker system, Cu $K\alpha$ radiation), the sample displacement was first refined against the silicon standard. The sample displacement was then fixed, and the relevant phases were then refined. For each phase, lattice parameters, size broadening, and atomic thermal parameters were refined. A 10-term polynomial was used to fit the background.

High-resolution SXR D datasets were analyzed in a similar way to identify the cation occupancy for the $\text{Ca}_x\text{M}_{2-x}\text{N}_2$ phase in each sample ($M = \text{Zr, Hf}$). Cubic ZrN ($Fm\bar{3}m$) was used as a starting model, with Ca and Zr or Hf on the cation site with 50% occupancy each. Cation occupancy (x) was constrained to equal anion occupancy (i.e., $\text{Ca} + M = \text{N}$) during refinements. The anion site was fixed at full occupancy. The atomic displacement parameters were refined

isotropically. Other relevant phases were also added to the model, and their lattice parameters, size broadening (Lorentzian), and atomic thermal parameters were refined. A broad background peak from the quartz capillary was modeled with a Lorentzian function, and the remaining background was modeled with a 10-term polynomial. The datasets were collected without an internal standard, and sample displacement was not refined during analysis.

Due to the number and positional overlap of intermediates during the sequential refinements, several variables were fixed to better compare phase fractions. Thermal displacement parameters were fixed at 1 \AA^2 for each phase to better account for changes in peak intensity during the reaction. Atoms were fixed at full occupancy for each site. RS phases were modeled as ZrN (i.e., metal site mixing was not refined). Crystalline size domain was fixed at 200 nm (as modeled using a Lorentzian polynomial) for most phases, except the ZrNCl and RS phases, which exhibited noticeable peak broadening. ZrNCl was refined using thermal displacement parameters were fixed at 20 \AA^2 and anisotropic size broadening. Size broadening for RS phases was manually refined from the final scan in the sequence and fixed for all other scans (crystallite size ca. 7 nm). In order to compare the relative fractions of phases determined from Rietveld calculations, a weighted scale factor (W.S.F.) is defined as $Q_p = S_p \cdot V_p \cdot M_p$ where Q_p = weighted scale factor of phase p , S_p is scale factor calculated from Rietveld, V_p is the volume of the unit cell, and M_p is the atomic mass of the unit cell. It should be noted that we omit the Brindley coefficient for microabsorption correction in our calculation of W.S.F. due to the unreliable refinement of particle sizes for individual phases. Amorphous material and product lost as vapor are not accounted for in the sequential refinement, hence we use the W.S.F. instead of relative wt% or mol%. We reference all phases by their nominal stoichiometric formula; however, the actual chemical formula may be distinct from the written formula as XRD data alone cannot typically resolve nonstoichiometric compounds.

Thermodynamic analysis

Thermodynamic calculations were performed using DFT-computed values and tools from the Materials Project (v2022.10.28) and pymatgen (v2023.9.10).^{56,68} Reaction energies were calculated

from the Gibbs formation energies as a function of temperature, using the method of Bartel, et al.⁶² Chemical potential diagrams were generated in the method of Yokokawa²¹ as detailed by Todd, et al.²² and implemented in pymatgen. Mg_2NCl is calculated to be +0.02 eV/atom metastable relative to the binaries, which is within DFT error of the convex hull. We therefore applied a small correction to bring the phase to the hull, allowing for visualization in the chemical potential diagrams. All other phases shown in Figures 6 and S21-S23 are calculated to be stable.

Thermodynamic analysis of disorder in CaZrN_2

To produce a training set for the cluster expansion, a number of DFT calculations were conducted using VASP.⁶⁹ The PBE functional was used within the projector-augmented wave method.⁷⁰ A planewave cutoff of 400 eV was used. K-point densities were used such that the total energies were converged within 1 meV/atom. All structural degrees of freedom were allowed to be optimized within the structural relaxation (ie. volume, cell shape, atom positions). Structures were generated using the pylada software.⁷¹ To produce symmetry-inequivalent supercells, Hermite Normal Form transformation matrices were constructed using an algorithm developed by Hart and Forcade.⁷² The transformation matrices were applied to the RS primitive cell to produce supercells with varying dimensions. The supercells were then decorated with different atomic orderings to make varying CaZrN_2 configurations.

The Alloy Theoretic Automated Toolkit (ATAT)^{73,74} was employed to fit a cluster expansion. To ensure that the cluster expansion was properly representing the highly ordered configurations, we exhaustively enumerated all 8-atom and 12-atom CaZrN_2 configurations and included them in the training set. In total, the training set was made up of 70 symmetry inequivalent CaZrN_2 configurations, ranging in size from 8 to 24-atoms. A cross validation score of 10.4 meV/atom was obtained. Considering that the training set had an energy range of 324 meV/atom, we deemed a 10.4 meV/atom cross validation score to be sufficiently small. The energies of all 37,883 24-atom CaZrN_2 configurations were predicted using the fitted cluster expansion.

To ensemble average the XRD patterns, first the partition function, Z , was calculated using all

37,883 24-atom configurations

$$Z(T) = \sum_i^{37,883} e^{-E_i/k_B T}. \quad (8)$$

Here, i is the index of the configuration, E_i is the total energy of the i th configuration, k_B is Boltzmann's constant, and T is the absolute temperature. The temperature-dependent probability of each configuration, $P_i(T)$, was then determined using the following equation

$$P_i(T) = \frac{e^{-E_i/k_B T}}{Z(T)}. \quad (9)$$

Finally, the intensity of the ensemble-averaged XRD, I , was calculated as a function of temperature and wavenumber, Q :

$$I(Q, T) = \sum_i^n (I_i(Q) \cdot P_i(T)). \quad (10)$$

For a justification of ensemble averaging XRD patterns in the above way, see Jones et. al.⁷⁵ The powder XRD pattern for each structure was generated with a Cu K_α wavelength using pymatgen.⁶⁸

Acknowledgements

The authors thank Paul Todd and Akira Miura for helpful discussions. This work was supported primarily by the National Science Foundation (DMR-2210780). The authors thank the Analytical Resources Core at Colorado State University for instrument access and training (RRID: SCR_021758). Use of the Advanced Photon Source at Argonne National Laboratory was supported by the U. S. Department of Energy, Office of Science, Office of Basic Energy Sciences, under Contract No. DE-AC02-06CH11357. Work conducted at Lawrence Berkeley National Laboratory was supported as part of GENESIS: A Next Generation Synthesis Center, an Energy Frontier Research Center funded by the U.S. Department of Energy, Office of Science, Basic Energy Sciences under Award Number DE-SC0019212. This research used resources of the National Energy Research Scientific Computing Center (NERSC), a U.S. Department of Energy Office of Science User Facility operated under Contract No. DE-AC02-05CH11231. This work was authored in part at

the National Renewable Energy Laboratory (NREL), operated by Alliance for Sustainable Energy, LLC, for the U.S. Department of Energy (DOE) under Contract No. DE-AC36-08GO28308. Funding for work conducted at NREL was provided by DOE Basic Energy Sciences Early Career Award “Kinetic Synthesis of Metastable Nitrides”. The views expressed in the article do not necessarily represent the views of the DOE or the U.S. Government. The U.S. Government retains and the publisher, by accepting the article for publication, acknowledges that the U.S. Government retains a nonexclusive, paid-up, irrevocable, worldwide license to publish or reproduce the published form of this work, or allow others to do so, for U.S. Government purposes.

Author Contributions

C.L.R. and J.R.N. conceptualized the project. C.L.R., E.N.S., B.C.M., and G.T.T. conducted syntheses and measured PXRD. D.C.A. conducted optical property measurements. J.R.G. conducted X-ray photoelectron spectroscopy measurements with support from A.L.P. The remote experiments were set up by beamline scientist A.A.Y., enabling C.L.R. to remotely control the data collection and conduct analysis. R.C.M. and C.L.R. conducted scanning electron microscopy and energy dispersive X-ray spectroscopy measurements. C.L.R. and M.J.M. conducted thermodynamic reaction calculations with support from K.A.P. and J.R.N. A.N. conducted thermodynamic modeling of cation disorder with support from E.T. and V.S., A.L.P., A.Z., and J.R.N. supervised and supported the project.

References

- (1) Kovnir, K. Predictive synthesis. *Chemistry of Materials* **2021**, *33*, 4835–4841.
- (2) Neilson, J. R.; McDermott, M. J.; Persson, K. A. Modernist materials synthesis: Finding thermodynamic shortcuts with hyperdimensional chemistry. *Journal of Materials Research* **2023**, 1–9.

- (3) Alberi, K.; Nardelli, M. B.; Zakutayev, A.; Mitas, L.; Curtarolo, S.; Jain, A.; Fornari, M.; Marzari, N.; Takeuchi, I.; Green, M. L.; others The 2019 materials by design roadmap. *Journal of Physics D: Applied Physics* **2018**, *52*, 013001.
- (4) Sun, W.; Bartel, C. J.; Arca, E.; Bauers, S. R.; Matthews, B.; Orvañanos, B.; Chen, B.-R.; Toney, M. F.; Schelhas, L. T.; Tumas, W.; others A map of the inorganic ternary metal nitrides. *Nature Materials* **2019**, *18*, 732–739.
- (5) Walters, L. N.; Zhang, C.; Dravid, V. P.; Poeppelmeier, K. R.; Rondinelli, J. M. First-Principles Hydrothermal Synthesis Design to Optimize Conditions and Increase the Yield of Quaternary Heteroanionic Oxychalcogenides. *Chemistry of Materials* **2021**, *33*, 2726–2741.
- (6) Gautier, R.; Zhang, X.; Hu, L.; Yu, L.; Lin, Y.; Sunde, T. O.; Chon, D.; Poeppelmeier, K. R.; Zunger, A. Prediction and accelerated laboratory discovery of previously unknown 18-electron ABX compounds. *Nature chemistry* **2015**, *7*, 308–316.
- (7) Raccuglia, P.; Elbert, K. C.; Adler, P. D.; Falk, C.; Wenny, M. B.; Mollo, A.; Zeller, M.; Friedler, S. A.; Schrier, J.; Norquist, A. J. Machine-learning-assisted materials discovery using failed experiments. *Nature* **2016**, *533*, 73–76.
- (8) Altman, A. B.; Tamerius, A. D.; Koocher, N. Z.; Meng, Y.; Pickard, C. J.; Walsh, J. P.; Rondinelli, J. M.; Jacobsen, S. D.; Freedman, D. E. Computationally directed discovery of MoBi₂. *Journal of the American Chemical Society* **2020**, *143*, 214–222.
- (9) Greenaway, A. L.; Ke, S.; Culman, T.; Talley, K. R.; Mangum, J. S.; Heinselman, K. N.; Kingsbury, R. S.; Smaha, R. W.; Gish, M. K.; Miller, E. M.; others Zinc Titanium Nitride Semiconductor toward Durable Photoelectrochemical Applications. *Journal of the American Chemical Society* **2022**, *144*, 13673–13687.
- (10) Heinselman, K. N.; Lany, S.; Perkins, J. D.; Talley, K. R.; Zakutayev, A. Thin Film Synthesis of Semiconductors in the Mg–Sb–N Materials System. *Chemistry of Materials* **2019**, *31*, 8717–8724.

- (11) Hinuma, Y.; Hatakeyama, T.; Kumagai, Y.; Burton, L. A.; Sato, H.; Muraba, Y.; Iimura, S.; Hiramatsu, H.; Tanaka, I.; Hosono, H.; others Discovery of earth-abundant nitride semiconductors by computational screening and high-pressure synthesis. *Nature communications* **2016**, *7*, 1–10.
- (12) Gvozdetskyi, V.; Bhaskar, G.; Batuk, M.; Zhao, X.; Wang, R.; Carnahan, S. L.; Hanrahan, M. P.; Ribeiro, R. A.; Canfield, P. C.; Rossini, A. J.; others Computationally driven discovery of a family of layered LiNiB polymorphs. *Angewandte Chemie International Edition* **2019**, *58*, 15855–15862.
- (13) Zakutayev, A.; Zhang, X.; Nagaraja, A.; Yu, L.; Lany, S.; Mason, T. O.; Ginley, D. S.; Zunger, A. Theoretical prediction and experimental realization of new stable inorganic materials using the inverse design approach. *Journal of the American Chemical Society* **2013**, *135*, 10048–10054.
- (14) Woods-Robinson, R.; Stevanović, V.; Lany, S.; Heinselman, K. N.; Horton, M. K.; Persson, K. A.; Zakutayev, A. Role of disorder in the synthesis of metastable zinc zirconium nitrides. *Physical Review Materials* **2022**, *6*, 043804.
- (15) Chen, B.-R.; Lany, S.; Kelly, L. L.; Arca, E.; Iguchi, Y.; Perkins, J. D.; Yanagi, H.; Toney, M. F.; Schelhas, L. T.; Zakutayev, A. Antimony nitride discovered by theoretical structure prediction, rapid thermal annealing, and in situ X-ray diffraction. *Cell Reports Physical Science* **2022**, *3*.
- (16) McDermott, M. J.; McBride, B. C.; Regier, C. E.; Tran, G. T.; Chen, Y.; Corrao, A. A.; Galant, M. C.; Kamm, G. E.; Bartel, C. J.; Chapman, K. W.; others Assessing Thermodynamic Selectivity of Solid-State Reactions for the Predictive Synthesis of Inorganic Materials. *ACS Central Science* **2023**,
- (17) Shoemaker, D. P.; Hu, Y.-J.; Chung, D. Y.; Halder, G. J.; Chupas, P. J.; Soderholm, L.; Mitchell, J.; Kanatzidis, M. G. In situ studies of a platform for metastable inorganic crystal

- growth and materials discovery. *Proceedings of the National Academy of Sciences* **2014**, *111*, 10922–10927.
- (18) Haynes, A. S.; Stoumpos, C. C.; Chen, H.; Chica, D.; Kanatzidis, M. G. Panoramic synthesis as an effective materials discovery tool: the system Cs/Sn/P/Se as a test case. *Journal of the American Chemical Society* **2017**, *139*, 10814–10821.
- (19) McClain, R.; Malliakas, C. D.; Shen, J.; He, J.; Wolverton, C.; González, G. B.; Kanatzidis, M. G. Mechanistic insight of KBiQ₂ (Q= S, Se) using panoramic synthesis towards synthesis-by-design. *Chemical Science* **2021**, *12*, 1378–1391.
- (20) Ito, H.; Shitara, K.; Wang, Y.; Fujii, K.; Yashima, M.; Goto, Y.; Moriyoshi, C.; Rosero-Navarro, N. C.; Miura, A.; Tadanaga, K. Kinetically Stabilized Cation Arrangement in Li₃YCl₆ Superionic Conductor during Solid-State Reaction. *Advanced Science* **2021**, *8*, 2101413.
- (21) Yokokawa, H. Generalized chemical potential diagram and its applications to chemical reactions at interfaces between dissimilar materials. *Journal of phase equilibria* **1999**, *20*, 258–287.
- (22) Todd, P. K.; McDermott, M. J.; Rom, C. L.; Corrao, A. A.; Denney, J. J.; Dwaraknath, S. S.; Khalifah, P. G.; Persson, K. A.; Neilson, J. R. Selectivity in Yttrium manganese oxide synthesis via local chemical potentials in hyperdimensional phase space. *Journal of the American Chemical Society* **2021**, *143*, 15185–15194.
- (23) “Bond Dissociation Energies in Diatomic Molecules” in *CRC Handbook of Chemistry and Physics*, 104th Edition (Internet Version 2023). https://hbcpc.chemnetbase.com/documents/09_04/09_04_0001.xhtml?dswid=6263.
- (24) Greenaway, A. L.; Melamed, C. L.; Tellekamp, M. B.; Woods-Robinson, R.; Toberer, E. S.; Neilson, J. R.; Tamboli, A. C. Ternary nitride materials: Fundamentals and emerging device applications. *Annual Review of Materials Research* **2021**, *51*, 591–618.

- (25) Niewa, R.; Jacobs, H. Group V and VI alkali nitridometalates: a growing class of compounds with structures related to silicate chemistry. *Chemical reviews* **1996**, *96*, 2053–2062.
- (26) Zakutayev, A.; Bauers, S. R.; Lany, S. Experimental Synthesis of Theoretically Predicted Multivalent Ternary Nitride Materials. *Chemistry of Materials* **2022**, *34*, 1418–1438.
- (27) Elder, S.; DiSalvo, F.; Topor, L.; Navrotsky, A. Thermodynamics of ternary nitride formation by ammonolysis: application to lithium molybdenum nitride (LiMoN₂), sodium tungsten nitride (Na₃WN₃), and sodium tungsten oxide nitride (Na₃WO₃N). *Chemistry of materials* **1993**, *5*, 1545–1553.
- (28) Rognerud, E. G.; Rom, C. L.; Todd, P. K.; Singstock, N. R.; Bartel, C. J.; Holder, A. M.; Neilson, J. R. Kinetically controlled low-temperature solid-state metathesis of manganese nitride Mn₃N₂. *Chemistry of Materials* **2019**, *31*, 7248–7254.
- (29) Gharavi, M. A.; Armiento, R.; Alling, B.; Eklund, P. Theoretical study of phase stability, crystal and electronic structure of MeMgN₂ (Me= Ti, Zr, Hf) compounds. *Journal of materials science* **2018**, *53*, 4294–4305.
- (30) Sarmiento-Perez, R.; Cerqueira, T. F.; Körbel, S.; Botti, S.; Marques, M. A. Prediction of stable nitride perovskites. *Chemistry of Materials* **2015**, *27*, 5957–5963.
- (31) Ching, W.; Mo, S.-D.; Tanaka, I.; Yoshiya, M. Prediction of spinel structure and properties of single and double nitrides. *Physical Review B* **2001**, *63*, 064102.
- (32) Greenaway, A. L.; Loutris, A. L.; Heinselman, K. N.; Melamed, C. L.; Schnepf, R. R.; Tellekamp, M. B.; Woods-Robinson, R.; Sherbondy, R.; Bardgett, D.; Bauers, S.; others Combinatorial synthesis of magnesium tin nitride semiconductors. *Journal of the American Chemical Society* **2020**, *142*, 8421–8430.
- (33) Kawamura, F.; Imura, M.; Murata, H.; Yamada, N.; Taniguchi, T. Synthesis of a Novel

- Rocksalt-Type Ternary Nitride Semiconductor MgSnN_2 Using the Metathesis Reaction Under High Pressure. *European Journal of Inorganic Chemistry* **2020**, 2020, 446–451.
- (34) Kawamura, F.; Murata, H.; Imura, M.; Yamada, N.; Taniguchi, T. Synthesis of CaSnN_2 via a high-pressure metathesis reaction and the properties of II-Sn- N_2 (II= Ca, Mg, Zn) semiconductors. *Inorganic Chemistry* **2021**, 60, 1773–1779.
- (35) Bauers, S. R.; Holder, A.; Sun, W.; Melamed, C. L.; Woods-Robinson, R.; Mangum, J.; Perkins, J.; Tumas, W.; Gorman, B.; Tamboli, A.; others Ternary nitride semiconductors in the rocksalt crystal structure. *Proceedings of the National Academy of Sciences* **2019**, 116, 14829–14834.
- (36) Rom, C. L.; Fallon, M. J.; Wustrow, A.; Prieto, A. L.; Neilson, J. R. Bulk Synthesis, Structure, and Electronic Properties of Magnesium Zirconium Nitride Solid Solutions. *Chemistry of Materials* **2021**, 33, 5345–5354.
- (37) Li, X.; Wang, X.; Han, Y.; Jing, X.; Huang, Q.; Kuang, X.; Gao, Q.; Chen, J.; Xing, X. High-dielectric-permittivity layered nitride CaTiN_2 . *Chemistry of Materials* **2017**, 29, 1989–1993.
- (38) Gregory, D.; Barker, M.; Edwards, P.; Siddons, D. Synthesis and structure of the new ternary nitride SrTiN_2 . *Inorganic chemistry* **1998**, 37, 3775–3778.
- (39) Gregory, D.; Barker, M.; Edwards, P.; Siddons, D. Synthesis and structure of two new layered ternary nitrides, SrZrN_2 and SrHfN_2 . *Inorganic chemistry* **1996**, 35, 7608–7613.
- (40) Shiraishi, A.; Kimura, S.; He, X.; Watanabe, N.; Katase, T.; Ide, K.; Minohara, M.; Matsuzaki, K.; Hiramatsu, H.; Kumigashira, H.; others Design, Synthesis, and Optoelectronic Properties of the High-Purity Phase in Layered AETMN_2 (AE= Sr, Ba; TM= Ti, Zr, Hf) Semiconductors. *Inorganic chemistry* **2022**, 61, 6650–6659.
- (41) Shannon, R. T.; Prewitt, C. T. Effective ionic radii in oxides and fluorides. *Acta Crystallographica Section B: Structural Crystallography and Crystal Chemistry* **1969**, 25, 925–946.

- (42) Orisakwe, E.; Fontaine, B.; Gregory, D. H.; Gautier, R.; Halet, J.-F. Theoretical study on the structural, electronic and physical properties of layered alkaline-earth-group-4 transition-metal nitrides $AEMN_2$. *RSC advances* **2014**, *4*, 31981–31987.
- (43) Hunting, J. L.; Szymanski, M. M.; Johnson, P. E.; Kellar, C. B.; DiSalvo, F. J. The synthesis and structural characterization of the new ternary nitrides: Ca_4TiN_4 and Ca_5NbN_5 . *Journal of Solid State Chemistry* **2007**, *180*, 31–40.
- (44) Masood, H.; Yunus, R.; Choong, T. S.; Rashid, U.; Yap, Y. H. T. Synthesis and characterization of calcium methoxide as heterogeneous catalyst for trimethylolpropane esters conversion reaction. *Applied Catalysis A: General* **2012**, *425*, 184–190.
- (45) Schneider, J. D.; Agocs, D. B.; Prieto, A. L. Design of a Sample Transfer Holder to Enable Air-Free X-ray Photoelectron Spectroscopy. *Chemistry of Materials* **2020**, *32*, 8091–8096.
- (46) Fairley, N.; Fernandez, V.; Richard-Plouet, M.; Guillot-Deudon, C.; Walton, J.; Smith, E.; Flahaut, D.; Greiner, M.; Biesinger, M.; Tougaard, S.; others Systematic and collaborative approach to problem solving using X-ray photoelectron spectroscopy. *Applied Surface Science Advances* **2021**, *5*, 100112.
- (47) Coelho, A. A. TOPAS and TOPAS-Academic: an optimization program integrating computer algebra and crystallographic objects written in C++. *Journal of Applied Crystallography* **2018**, *51*, 210–218.
- (48) Azdad, Z.; Marot, L.; Moser, L.; Steiner, R.; Meyer, E. Valence band behaviour of zirconium oxide, Photoelectron and Auger spectroscopy study. *Scientific reports* **2018**, *8*, 16251.
- (49) Christensen, A. A Neutron Diffraction Investigation on Single Crystals of Titanium Carbide, Titanium Nitride, and Zirconium Nitride. *Acta Chemica Scandinavica* **1975**, *29a*, 563–564.
- (50) Aigner, K.; Lengauer, W.; Rafaja, D.; Ettmayer, P. Lattice parameters and thermal expansion

- of $\text{Ti}(\text{C}_x\text{N}_{1-x})$, $\text{Zr}(\text{C}_x\text{N}_{1-x})$, $\text{Hf}(\text{C}_x\text{N}_{1-x})$ and TiN_{1-x} from 298 to 1473 K as investigated by high-temperature X-ray diffraction. *Journal of alloys and compounds* **1994**, *215*, 121–126.
- (51) Martinolich, A. J.; Kurzman, J. A.; Neilson, J. R. Circumventing diffusion in kinetically controlled solid-state metathesis reactions. *Journal of the American Chemical Society* **2016**, *138*, 11031–11037.
- (52) Gillan, E. G.; Kaner, R. B. Synthesis of refractory ceramics via rapid metathesis reactions between solid-state precursors. *Chemistry of materials* **1996**, *8*, 333–343.
- (53) Gregory, D. H.; Barker, M. G.; Siddons, D. J.; Edwards, P. P.; Slaski, M. Synthesis, Structure and Magnetic Properties of the Group IV Ternary Nitrides, AMN_2 (A = Alkaline Earth Metal, M = Transition Metal). *MRS Online Proceedings Library (OPL)* **1998**, 547.
- (54) Todd, P. K.; Fallon, M. J.; Neilson, J. R.; Zakutayev, A. Two-step solid-state synthesis of ternary nitride materials. *ACS Materials Letters* **2021**, *3*, 1677–1683.
- (55) Houska, C. Thermal expansion and atomic vibration amplitudes for TiC, TiN, ZrC, ZrN, and pure tungsten. *Journal of Physics and Chemistry of Solids* **1964**, *25*, 359–366.
- (56) Jain, A.; Ong, S. P.; Hautier, G.; Chen, W.; Richards, W. D.; Dacek, S.; Cholia, S.; Gunter, D.; Skinner, D.; Ceder, G.; others Commentary: The Materials Project: A materials genome approach to accelerating materials innovation. *APL materials* **2013**, *1*, 011002.
- (57) McDermott, M. J.; Dwaraknath, S. S.; Persson, K. A. A graph-based network for predicting chemical reaction pathways in solid-state materials synthesis. *Nature communications* **2021**, *12*, 1–12.
- (58) Novick, A.; Nguyen, Q.; Garnett, R.; Toberer, E.; Stevanović, V. The Mixing Thermodynamics and Local Structure of High-entropy Alloys from Randomly Sampled Ordered Configurations. *arXiv preprint arXiv:2211.13066* **2022**,

- (59) Schnepf, R. R.; Cordell, J. J.; Tellekamp, M. B.; Melamed, C. L.; Greenaway, A. L.; Mis, A.; Brennecke, G. L.; Christensen, S.; Tucker, G. J.; Toberer, E. S.; others Utilizing site disorder in the development of new energy-relevant semiconductors. *ACS Energy Letters* **2020**, *5*, 2027–2041.
- (60) Blanton, E. W.; He, K.; Shan, J.; Kash, K. Characterization and control of ZnGeN₂ cation lattice ordering. *Journal of Crystal Growth* **2017**, *461*, 38–45.
- (61) Schnepf, R. R.; Martinez, A. D.; Mangum, J. S.; Schelhas, L. T.; Toberer, E. S.; Tamboli, A. C. Disorder-tunable ZnGeP₂ for epitaxial top cells on Si. 2019 IEEE 46th Photovoltaic Specialists Conference (PVSC). 2019; pp 1052–1055.
- (62) Bartel, C. J.; Millican, S. L.; Deml, A. M.; Rumptz, J. R.; Tumas, W.; Weimer, A. W.; Lany, S.; Stevanović, V.; Musgrave, C. B.; Holder, A. M. Physical descriptor for the Gibbs energy of inorganic crystalline solids and temperature-dependent materials chemistry. *Nature Communications* **2018**, *9*, 4168.
- (63) Hadenfeldt, C.; Herdejürgen, H. Darstellung und Kristallstruktur der Calciumnitridhalogenide Ca₂NCl und Ca₂NBr. *Zeitschrift für anorganische und allgemeine Chemie* **1987**, *545*, 177–183.
- (64) Li, Y.; George, J.; Liu, X.; Dronskowski, R. Synthesis, structure determination and electronic structure of magnesium nitride chloride, Mg₂NCl. *Zeitschrift für anorganische und allgemeine Chemie* **2015**, *641*, 266–269.
- (65) Williams, D. B. G.; Lawton, M. Drying of organic solvents: quantitative evaluation of the efficiency of several desiccants. *The Journal of organic chemistry* **2010**, *75*, 8351–8354.
- (66) Wang, J.; Toby, B. H.; Lee, P. L.; Ribaud, L.; Antao, S. M.; Kurtz, C.; Ramanathan, M.; Von Dreele, R. B.; Beno, M. A. A dedicated powder diffraction beamline at the Advanced Photon Source: Commissioning and early operational results. *Review of Scientific Instruments* **2008**, *79*, 085105.

- (67) Chupas, P. J.; Chapman, K. W.; Kurtz, C.; Hanson, J. C.; Lee, P. L.; Grey, C. P. A versatile sample-environment cell for non-ambient X-ray scattering experiments. *Journal of Applied Crystallography* **2008**, *41*, 822–824.
- (68) Ong, S. P.; Richards, W. D.; Jain, A.; Hautier, G.; Kocher, M.; Cholia, S.; Gunter, D.; Chevrier, V. L.; Persson, K. A.; Ceder, G. Python Materials Genomics (pymatgen): A robust, open-source python library for materials analysis. *Computational Materials Science* **2013**, *68*, 314–319.
- (69) Kresse, G.; Furthmüller, J. Efficiency of ab-initio total energy calculations for metals and semiconductors using a plane-wave basis set. *Comput. Mater. Sci.* **1996**, *6*, 15.
- (70) Blöchl, P. E. Projector augmented-wave method. *Phys. Rev. B* **1994**, *50*, 17953–17979.
- (71) d’Avezac, M.; Graf, P.; Paudal, T.; Peng, H.; Zhang, L.; Stephen, S.; Stevanovic, V. Pylada: a Comprehensive Python Framework for Preparing, Running, Monitoring, Analyzing, and Archiving High Throughput First Principles Calculations. *GitHub repository* **2010**,
- (72) Hart, G. L. W.; Forcade, R. W. Algorithm for generating derivative structures. *Physical Review B* **2008**, *77*, 224115.
- (73) Van De Walle, A.; Asta, M.; Ceder, G. The alloy theoretic automated toolkit: A user guide. *Calphad* **2002**, *26*, 539–553.
- (74) Van De Walle, A.; Ceder, G. Automating first-principles phase diagram calculations. *Journal of Phase Equilibria* **2002**, *23*, 348.
- (75) Jones, E. B.; Stevanović, V. The glassy solid as a statistical ensemble of crystalline microstates. *npj Computational Materials* **2020**, *6*, 56.

TOC Graphic

